Available online at www.sciencedirect.com
ScienceDirect
Journal of Magnetic Resonance 182 (2006) 315–324
JMR Journal of Magnetic Resonance
www.elsevier.com/locate/jmr

# Sensitivity to local dipole fields in the CRAZED experiment: An approach to bright spot MRI

Cornelius Faber [a,b,*], Carolin Heil [a], Benjamin Zahneisen [a], David Z. Balla [a], Richard Bowtell [b]

[a] Department of Experimental Physics 5, University of Würzburg, 97074 Würzburg, Germany
[b] Sir Peter Mansfield Magnetic Resonance Centre, School of Physics and Astronomy, University of Nottingham, University Park, NG7 2RD Nottingham, UK

Received 12 January 2006; revised 4 April 2006
Available online 22 May 2006

**Abstract**

Local dipole fields such as those created by small iron-oxide particles are used to produce regions of low intensity (dark contrast) in many molecular magnetic resonance imaging applications. We have investigated, with computer simulations and experiments at 17.6 T, how the COSY revamped with asymmetric *z*-gradient echo detection (CRAZED) experiment that selects intermolecular double-quantum coherences can also be used to visualize such local dipole fields. Application of the coherence-selection gradient pulses parallel to the main magnetic field produced similar, dark contrast as conventional gradient echo imaging. Application of the gradient along the magic angle leads to total loss of signal intensity in homogeneous samples. In the presence of local dipole fields, the contrast was inverted and bright signals from the dipoles were observed over a very low background. Both simulations and experiments showed that the signal strongly decreased when a phase-cycle suppressing single-quantum coherences was employed. Therefore, we conclude that most of the signal comes from directly refocused magnetization or intermolecular single-quantum coherences. Finally, we demonstrate that bright contrast from local dipole fields can also be obtained, when the pair of coherence-selection gradient pulses is deliberately mismatched. Both methods allowed visualization of local dipole fields in phantoms in experimental times of about 3 min.


*Keywords:* DDF; iMQC; NMR imaging; Bright contrast; SPIO

## 1. Introduction

Since, applications of molecular imaging have become feasible in magnetic resonance imaging (MRI), considerable interest has been dedicated to local dipole fields. The most common strategy for visualizing cellular populations or molecular targets is to label them with small paramagnetic iron-oxide particles (SPIOs). The dipole field originating from the SPIOs locally changes the contrast in imaging experiments. In particular in gradient echo experiments magnetization is dephased in a surrounding area large compared to the actual size of the SPIO. Thus, micrometer-sized particles can be visualized even at moderate magnetic field strengths and spatial resolution, as used for example in clinical MRI systems [1,2]. The disadvantage of this approach in molecular imaging is that negative contrast is created so that in experiments where SNR is low or other sources of strong signal attenuation are present, the effects of the structure of interest may well be obscured. A variety of methods have been proposed to allow inversion of the negative contrast so as to produce bright signal at the sites of interest. This has been, for example, achieved by deliberately mismatching gradient pulse pairs [3,4], or by using off-resonance refocusing pulses to exploit the frequency shift caused by the SPIOs [5]. In an alternative approach the CRAZED (COSY revamped with asymmetric *z*-gradient echo detection) experiment [6] has been shown to enhance the effects of magnetic nanoparticles and produce excellent contrast in tissue [7].

* Corresponding author. Fax: +49 931 888 5851.
*E-mail address:* faber@physik.uni-wuerzburg.de (C. Faber).

1090-7807/$ - see front matter © 2006 Elsevier Inc. All rights reserved.
doi:10.1016/j.jmr.2006.05.002

Here, we describe how the CRAZED sequence can be used to visualize local dipole fields and how positive contrast can thus be obtained.

## 2. Theory

### 2.1. Theoretical background

Every NMR experiment makes use of an equilibrium nuclear magnetization $M_0$ created by a polarizing field $B_0$, generally applied along the $z$-direction. This magnetization gives rise to a long range dipolar magnetic field $B_{\mathrm{DDF}}$ (DDF, for distant dipolar field) which, if $B_0 \gg \mu_0 M_0$, is given by [8]

$$\vec{B}_{\mathrm{DDF}}(\vec{r}) = \frac{\mu_0}{4\pi}\int \mathrm{d}^3 r' \frac{1-3\cos^2\theta}{2|\vec{r}-\vec{r}'|^3}\left[3M_z(\vec{r}')\hat{z} - \vec{M}(\vec{r}')\right], \qquad (1)$$

where $\hat{z}$ is the unit vector in the direction of $B_0$ and $\theta$ is the angle between $\hat{z}$ and, $(\vec{r}-\vec{r}')$, while $\vec{M}(\vec{r})$ characterises the spatial distribution of the magnetization. For an isotropic spherical sample the integral vanishes, and for cylindrical sample tubes in which the magnetization is uniformly distributed, as used in most NMR spectroscopy experiments, $B_{\mathrm{DDF}}$ is small and can be neglected, even at high polarizing fields. If $\vec{M}(\vec{r})$ is not isotropic, as for example in a structured sample, or after application of magnetic field gradients, $B_{\mathrm{DDF}}$ may no longer be negligible. An additional term then has to be taken into account in the Bloch equations. Neglecting relaxation and radiation damping, and considering a sample containing only one spin species, evolution of $\vec{M}(\vec{r})$ in the rotating frame is given by

$$\frac{\mathrm{d}\vec{M}(\vec{r},t)}{\mathrm{d}t} = \gamma\vec{M}(\vec{r},t)\times\left[\vec{B}_{\mathrm{DDF}}(\vec{r},t)+\vec{B}_{\mathrm{dip}}(\vec{r})\right] + D\nabla^2\vec{M}(\vec{r},t), \qquad (2)$$

where $\gamma$ is the magnetogyric ratio and $D$ the self diffusion coefficient. $\vec{B}_{\mathrm{dip}}(\vec{r})$ describes local field variations due to susceptibility differences, or magnetic dipoles in the sample (e.g. SPIOs). Long range field distortions caused for example by a bad shim will be neglected throughout this treatment. The time dependence of $B_{\mathrm{DDF}}$ makes Eq. (2) non-linear and a solution generally requires evaluation of the integral in Eq. (1) at all points inside the sample. Generally this has to be done numerically, making solution of Eq. (2) time-consuming, even if $B_{\mathrm{dip}}$ is neglected. Fourier-transforming Eq. (1) into $k$-space significantly simplifies the situation [8,9] since

$$\vec{B}_{\mathrm{DDF}}(\vec{k}) = \frac{1}{3}\mu_0\frac{3\left(\hat{k}\cdot\hat{z}\right)^2-1}{2}\left[3M_z(\vec{k})\hat{z}-\vec{M}(\vec{k})\right], \qquad (3)$$

where $\vec{B}_{\mathrm{DDF}}(\vec{k})$ is a local function and easily calculated. Analysis in $k$-space yields information on periodic structures in the sample and allows for observation of diffraction effects [10–13]. Furthermore, if $\vec{B}_{\mathrm{DDF}}(\vec{k})$ is a one-dimensional function of $\vec{k}$, it is also a local function in real space after inverse Fourier-transformation. For modulation along the direction, $\hat{s}$, it can be shown that in this situation [8]

$$\vec{B}_{\mathrm{DDF}}(s) = \frac{1}{3}\mu_0\frac{3(\hat{s}\cdot\hat{z})^2-1}{2}\left[3M_z(s)\hat{z}-\vec{M}(s)\right]. \qquad (4)$$

Experimentally, one-dimensional modulation of $\vec{M}(\vec{r})$ is achieved by application of strong magnetic field gradients. Manifestations of the DDF can be observed as multiple spin echoes or additional cross peaks in two-dimensional spectra [14,15] in experiments involving application of only two radio frequency (rf) pulses. The most common approach to carrying out MR imaging experiments based on signal originating from the DDF is via the CRAZED pulse sequence (Fig. 1) [16]. This uses a pair of unmatched gradient pulses flanking the second rf-pulse which refocus double-quantum-coherence-like signal. Since the magnitude of the refocused signal depends on Eq. (4), maximum intensity is obtained when $z$-gradient pulses are employed and no signal is detected if the gradients are applied along the magic angle (54.7°). As a result of this angular dependence, CRAZED signal can yield information about the structure of the sample, which is independent of the resolution in the acquired image. The influence of the sample geometry on the signal, as well as the dynamics of the CRAZED signal has been studied extensively [10–12,16–30]. In most imaging experiments, however, it has been assumed that the magnetization is modulated only along one dimension and thus, $B_{\mathrm{DDF}}$ is a local function in real space (Eq. (4)). This assumption does not hold, for example, for samples that are structured on the length scale of the modulation of magnetization or where significant effects due to $B_{\mathrm{dip}}$ cause the magnetization to be locally perturbed. In such situations, numerical solution of Eq. (2) in real space becomes very time-consuming. Alternatively $B_{\mathrm{DDF}}(r)$ can be obtained by Fourier-transformation of the solution of Eq. (3). In previous work, this strategy has been used to perform efficient simulations of signal originating from the DDF following different pulse sequences under various conditions [30–36].

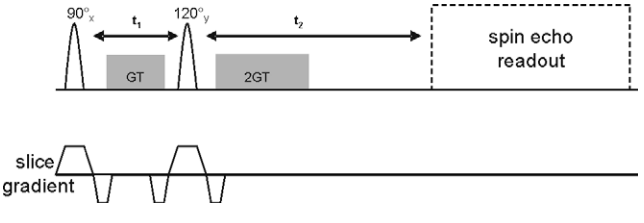


Fig. 1. CRAZED pulse sequence used in the experiments and simulations. Gaussian shapes indicate slice selective rf-pulses. Flip angle and phase are indicated above each pulse. Grey boxes indicate correlation gradients of strength, $G$, and duration, $T$. In all experiments and simulations $t_2 = 2t_1$. Simulations were performed until the end of the $t_2$-interval. In the experiments, signal was acquired with a symmetric spin echo read out ($TE/2$–π–$TE/2$).

### 2.2. CRAZED signal in presence of a significant local dipole field

Here, we investigate the behaviour of the CRAZED signal in the situation where local magnetic field gradients, as induced by susceptibility differences or paramagnetic particles, render the assumption of a one-dimensional modulation of the magnetization invalid. The modulating magnetic field gradients in the CRAZED sequence (Fig. 1) are applied along the $s$-direction. We neglect the diffusion term in Eq. (2) and assume that $T$ is very short, so that the gradient modulation is switched on instantaneously. Then immediately after the second rf-pulse, the magnetization is described by:

$$M_z(\vec{r}) = -M_0(\vec{r}) \sin\theta \cos\left(k_m s + \gamma B_{\mathrm{dip}}(\vec{r}) t_1\right), \tag{5}$$

and

$$M^+(\vec{r}) = \mathrm{i} M_0(\vec{r}) \left[ \frac{1+\cos\theta}{2} \mathrm{e}^{-\mathrm{i}\left(k_m s + \gamma B_{\mathrm{dip}}(\vec{r}) t_1\right)} + \frac{\cos\theta - 1}{2} \mathrm{e}^{\mathrm{i}\left(k_m s + \gamma B_{\mathrm{dip}}(\vec{r}) t_1\right)} \right] \mathrm{e}^{-\mathrm{i}2 k_m s}, \tag{6}$$

with $k_m = \gamma \mathrm{GT}$ and $M^+ = M_x + \mathrm{i} M_y$.

Subsequently the magnetization evolves according to Eq. (2), so that, ignoring relaxation, radiation damping, and diffusion

$$\frac{\mathrm{d}M_z}{\mathrm{d}t} = \frac{\mathrm{i}\gamma}{2} \left( M^+ \left( B^+_{\mathrm{DDF}} + B^+_{\mathrm{dip}} \right)^* - (M^+)^* \left( B^+_{\mathrm{DDF}} + B^+_{\mathrm{dip}} \right) \right), \tag{7}$$

$$\frac{\mathrm{d}M^+}{\mathrm{d}t} = \mathrm{i}\gamma M^+ \left( B^z_{\mathrm{DDF}} + B^z_{\mathrm{dip}} \right) + \mathrm{i}\gamma M_z \left( B^+_{\mathrm{DDF}} + B^+_{\mathrm{dip}} \right), \tag{8}$$

where all $M$ and $B$ terms are functions of $\vec{r}$.

In the laboratory frame the local dipole field originating from a SPIO is given by:

$$B^{\mathrm{lab}}_{\mathrm{dip},z} = c \frac{x^2 + y^2 - 2z^2}{r^5}, \tag{9}$$

$$B^{\mathrm{lab}}_{\mathrm{dip},x} = c \frac{x \cdot z}{r^5}, \tag{10}$$

$$B^{\mathrm{lab}}_{\mathrm{dip},y} = c \frac{y \cdot z}{r^5}. \tag{11}$$

For a small paramagnetic particle: $c = \frac{\mu_0 M}{4\pi}$, where $\mu_0$ is the vacuum permeability and $M$ the magnetic moment of the SPIO. For the dipole field originating from a volume $V$ with magnetic susceptibility differing by an amount $\Delta\chi$ from its surroundings (such as an air bubble) at field strength $B_0$

$$c = \frac{B_0 \Delta\chi V}{4\pi}. \tag{12}$$

In the rotating frame, the effects of the static component $B^+_{\mathrm{dip}}$ are averaged out in a first order approximation and thus can be neglected in Eqs. (2), (7), and (8). The longitudinal component is correctly described by Eq. (9).

We were not able to obtain an analytic solution for Eq. (8) with $B_{\mathrm{dip}}$ as described by Eq. (9). However, since $B_{\mathrm{dip}}$ depends on $r^{-3}$ three cases can be distinguished without explicitly solving Eq. (8):

1. Distant from the dipole (large $r$) $B_{\mathrm{dip}}$ only displays a small spatial variation, $|\nabla\left(\gamma \vec{B}_{\mathrm{dip}}\right)| \cdot t_1 \ll k_m$: the modulation imposed by $B_{\mathrm{dip}}$ becomes negligible and the corresponding terms can be dropped from Eq. (7). Signal evolution is then identical to that occurring in a CRAZED experiment in a homogeneous sample.
2. Close to the dipole (small $r$) $B_{\mathrm{dip}}$ shows a strong spatial variation, $|\nabla\left(\gamma \vec{B}_{\mathrm{dip}}\right)| \cdot t_1 \gg k_m$: the direction of modulation of magnetization is dominated by the effect of $B_{\mathrm{dip}}$ and changes over small length scales compared with the pitch of the modulation generated using the applied gradients.
3. At intermediate distance $\left|\nabla\left(\gamma \vec{B}_{\mathrm{dip}}\right)\right| \cdot t_1$ and $k_m$ are of the same order: local modulation of the magnetization due to $B_{\mathrm{dip}}$ interferes with the correlation gradient imposed modulation. Since modulation of the magnetization is not one-dimensional the normally assumed local nature of the DDF does not apply. In this case, signal evolution can not be understood easily. Therefore, we have used computer simulations to numerically solve Eq. (8) and calculate the expected signal.

## 3. Methods and experiments

### 3.1. Computer simulations

All simulations were carried out with the program package MATLAB (The MathWorks Inc., Natick, MA) on conventional personal computers. Signal evolution as described by Eq. (2) was calculated for the CRAZED sequence shown in Fig. 1. $B_{\mathrm{DDF}}$ and $M_{\mathrm{Diff}}$, describing changes in magnetization originating from diffusion, were calculated after Fourier-transformation in $k$-space, following the strategy proposed by Enss et al. [31]. Calculations with matrices of up to $128 \times 128 \times 64$ in size were performed. Simulations were carried out for a resonant frequency of 750 MHz for water ($D = 2.3 \times 10^{-9}\ \mathrm{m^2\ s^{-1}}$). A cylindrical sample geometry with radius, $r = 1.1$ mm ($xy$-plane), and height, $h = 2.3$ mm ($z$-axis), in a cube of $(2.3\ \mathrm{mm})^3$, and a cylinder with $r = 1.5$ mm and $h = 2.3$ mm, in a box of $(3.0\ \mathrm{mm})^2 \times 2.3$ mm were simulated using a 3D grid with 64 or 128 points per dimension. Modulation from the correlation gradients was switched on immediately (zero gradient pulse duration), prior to and after the second rf-pulse. Eq. (2) was solved by using a MATLAB differential equation solver (ode45) for different intervals $t_2 = 2 * t_1$. Phase cycling was implemented by adding the results of two calculations with alternating phase ($x$ and $-x$) of the first rf-pulse.

A dipole field originating from a SPIO or air bubble located at the origin with $B_{dip}$ as given by Eq. (9) was used. The scaling constant c was set to $10^{-16}$ T m$^3$ corresponding to a spherical inclusion with a diameter of 0.25 mm and $\Delta\chi = 9$ ppm. At the surface of a spherical air bubble $B_{dip}$ reaches its maximum value of $B_0\Delta\chi/3$ (see Eq. (12)). Therefore $B_{dip}$ was set to zero where its calculated value exceeded $B_{cutoff} = 5 \times 10^{-5}$ T. CPU-time needed for the simulations depended strongly on the value of $B_{dip}$. While simulation of a CRAZED sequence with $B_{dip} = 0$ took only ca. 10 min. for $t_1 = 10$ ms in a $64^3$ matrix, simulations with an additional dipole field took up to 30 h for a $128^2$ * 64 matrix.

Although the applied simulation strategy has previously been demonstrated to be very powerful for simulating signal evolution in homogeneous samples, grid resolution becomes a limiting factor in simulations with fine-structured samples or strongly varying fields. In its experimental implementation, the CRAZED sequence relies on averaging out unwanted signal over a (usually large) number of modulation lengths ($2\pi/k_m$) spanning every single voxel. Computer simulations have to provide at least four grid points per modulation [31]. Efficient suppression of unwanted signal is only achieved when averaging over multiples of one full modulation. For a structured sample this requirement is not met and the quality of averaging increases with the number of grid points per modulation. However, with a maximum number of 128 points per dimension this allowed only for coarse image resolution over a small field of view. For the simulation of $z$-modulated CRAZED, 16 grid points per modulation length were used (4 modulation lengths spanning 64 grid points) corresponding to a modulation length of 0.575 mm. For simulation of the case where modulation was applied along the magic angle, 16 grid points per modulation length were used in the $xy$-plane, resulting in a full in plane-modulation length of 0.2875 mm. These values are larger than those employed in the experiments, but still only samples with 3 or 2.3 mm diameter could be simulated in a reasonable time. It is important to note that the simulations do not exactly reproduce the geometry of the experiments and that the simulated correlation gradients are weaker than those used in the experiment. Therefore no quantitative comparisons between experimental and simulated data were carried out. In particular in the simulations, interference of $B_{dip}$ with gradient imposed modulation happens on a larger length scale than in the experiments. However, the simulations provide important qualitative insight into the interaction of the effects of the inhomogeneities and the DDF.

### 3.2. NMR imaging

All imaging experiments were performed using a Bruker Avance 750 widebore spectrometer (Bruker Biospin, Rheinstetten, Germany) equipped with a 200-mT/m gradient system with an inner diameter of 57 mm and a home-built 38 mm bird cage resonator. A phantom sample containing agar gel in a 15 ml centrifuge tube was used. 2 μm-sized, polyethylene-imine-coated iron oxide particles with an average saturation magnetization of 5000 A/m (Micromod, Rostock, Germany) were added to the gel. During cooling, air bubbles of varying size formed in the gel. Since the size of the bubbles' dipole moments strongly exceeded those of the SPIOs, local dipole fields from the bubbles dominated and effects from the SPIOs were only expected for clustered particles.

CRAZED images were acquired using the pulse sequence shown in Fig. 1. A slice-selective Gaussian $\pi/2$—pulse with a duration of 0.5 ms was used for excitation. Correlation gradient pulses (duration ratio 1:+2) both having the same amplitude were applied prior to and after the second rf-pulse so as to select double-quantum coherences (DQC). The flip angle, $\theta$, of the second rf-pulse (Gaussian shape, 0.5 ms duration) was set to $2\pi/3$ to maximize the DQC signal. A slice-selective Gaussian-shaped $\pi$-pulse with a duration of 0.5 ms was used for the spin echo readout. To refocus the signal from the $(-2)$-quantum coherences at the center of the sampling window, the refocusing time had to fulfill the condition $t_2 = 2t_1$ and was followed by a symmetric spin echo read out ($TE/2$–$\pi$–$TE/2$).

We performed three different types of CRAZED-like experiments which differed in the direction and the strength of the applied correlation gradients. The gradient pulse duration was 1 ms for the first pulse and 2 ms for the second pulse in all experiments. Since, the CRAZED signal is a function of the evolution time, $t_1$, between the first two rf-pulses, this time was varied between 3 and 12 ms. The FOV was set to $(15\text{ mm})^2$ and the slice thickness to 1 mm. For acquisition of conventional CRAZED images, the correlation gradients were applied along the direction of $B_0$, and the gradient strength of both gradient pulses was 100 mT/m. Other imaging parameters were: $TE = 40$ ms, $TR = 10$ s, 4 averages, matrix size $= 128 \times 128$. To remove signals originating from undesired coherence orders, a four-step phase cycling $(x, -x, y, -y)$ was applied to the first $\pi/2$ pulse along with a receiver phase cycle $\Phi_{rec} = (x, x, -x, -x)$. The four-step phase cycle removes effects from imperfect pulses and other experimental artifacts. Since ideal conditions are assumed to obtain in the simulations, a two-step phase cycle was sufficient.

For modulation along the magic angle (54.7°) the strength of the $z$-gradient applied during the correlation gradient pulses was set to 100 mT/m, while the strength of the transverse gradient during the same pulses was 141 mT/m. Images were acquired with a $TR$ of 3 s and a matrix size of $64 \times 64$ for different values of $TE$. Experiments were performed with and without a two-step phase cycle $(x, -x)$ applied to the first rf-pulse.

Additional experiments based on the modified CRAZED sequence were conducted with mismatched gradient pulse pairs. The gradient strength of the first gradient pulse was set to 100 mT/m, while the strength of the second gradient pulse was varied between 20 and 120 mT/m. These images were obtained with the following imaging parameters: $TE = 40$ ms, $TR = 3$ s, and matrix size $= 64 \times 64$.

For comparison, both gradient echo and high resolution spin echo images were also acquired. Parameters for the gradient echo experiments were: $TE = 10$ ms, $TR = 30$ ms, number of averages $= 32$, FOV $= (15\text{ mm})^2$, matrix size $= 256 \times 256$, and slice thickness $= 0.5$ mm. 2D spin echo images were acquired using the following imaging parameters: $TE = 15.5$ ms, $TR = 3$ s, number of averages $= 4$, FOV $= (15\text{ mm})^2$, matrix size $= 256 \times 256$. The in-plane resolution was 59 μm, the slice thickness 0.3 mm. 3D spin echo images of a 5 mm slab were obtained with 59 μm in-plane resolution and 0.156 mm slice thickness using a $TE$ of 15.5 ms, a $TR$ of 1.5 s, and a matrix size of $256 \times 256 \times 32$.

## 4. Results

### 4.1. Negative contrast from local dipole fields

To demonstrate the influence of $B_{dip}$ on the evolution of the magnetization we have simulated a CRAZED experiment without gradient-imposed modulation. Figs. 2a and b show contour plots of the longitudinal magnetization, $M_z$, in the central $y$–$z$-plane of the simulation grid, immediately after the second rf-pulse for $t_1 = 2$ ms (Fig. 2a) and $t_1 = 10$ ms (Fig. 2b). $M_z$ is modulated in a typical dipolar pattern with strong modulation along the $z$-axis and in the transverse plane, but zero modulation along the magic angle. Close to the dipole, the frequency of spatial modulation is high, but distant from the dipole, modulation decreases to zero. The extent of the region over which significant modulation occurs, depends on the length of the $t_1$-interval. While in Fig. 2a the modulation is confined to a region close to the dipole, in Fig. 2b the extent of modulation exceeds that of the simulated slab. The spatial extent of the modulation illustrates the length scale on which interference with gradient imposed modulation is to be expected in a CRAZED experiment. Figs. 2c and d show the corresponding $M^+$-values summed over all $z$-slices, representing the signal detected in the CRAZED image acquired after a signal growth time of $t_2 = 4$ ms (Fig. 2c), and $t_2 = 20$ ms (Fig. 2d). It is basically identical to the signal in a conventional gradient echo experiment except for the effect of the second rf-pulse in converting a small portion of the transverse magnetization into longitudinal magnetization. Close to the dipole, transverse magnetization is reduced and lower signal will be detected in the image. The size of the affected region grows with longer evolution times. Near the edge of the cylinder, beyond the reach of the dipole field, normal signal intensity is observed, because no phase cycle was applied to suppress SQC signal.

Fig. 3 shows $M_y$ summed over all $z$-slices for a simulated CRAZED experiment with gradient-imposed $z$-modulation with no dipole present (Fig. 3a) and in the presence of a dipole (Figs. 3b and c). A two-step phase cycle on the first rf-pulse was used to suppress directly refocused, or single-quantum-coherence-like, signal and thus enhance

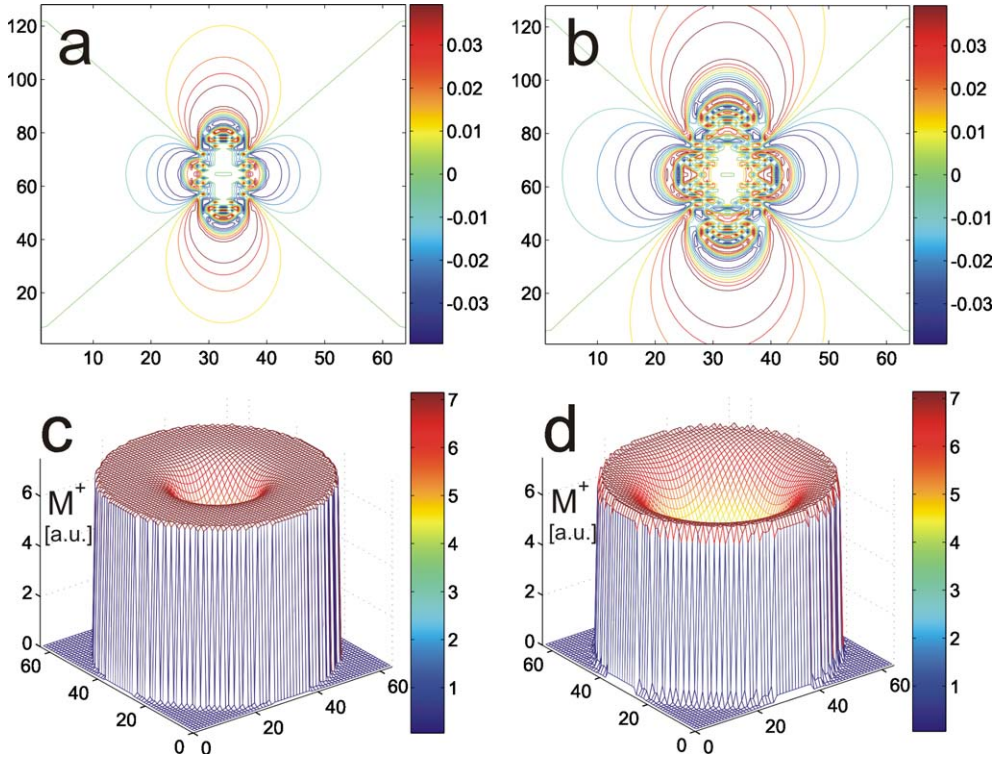


Fig. 2. Simulation of the CRAZED experiment with no correlation gradient applied ($G = 0$), over an $x$–$y$–$z$ grid of $64 \times 64 \times 128$ points, representing a box of $3 \times 3 \times 2.3$ mm$^3$ extent. No averaging or phase cycling was employed. (a and b) Contour plots of $M_z$ in the 32nd $yz$ plane immediately after the second rf-pulse, $t_1 = 2$ ms (a), $t_1 = 10$ ms (b). (c and d) $M^+$ summed over all $z$-slices after the $t_2$-interval, $t_1 = 2$ ms (c), $t_1 = 10$ ms (d).

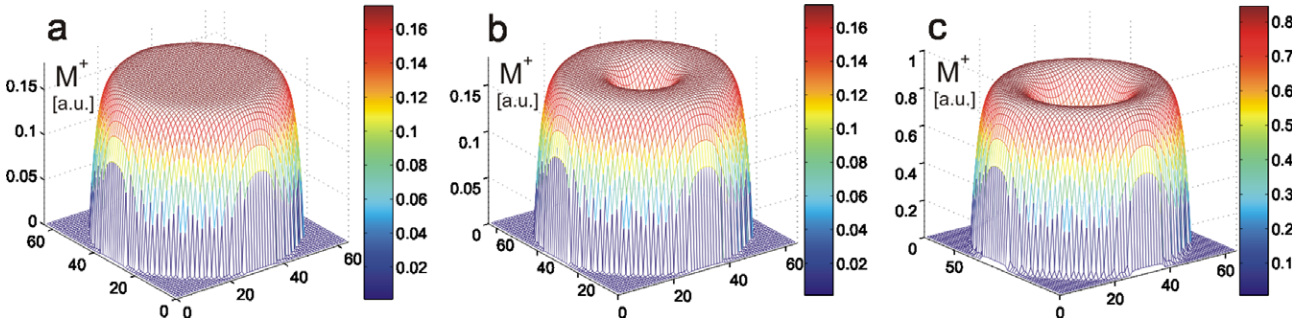


Fig. 3. Simulation of the CRAZED experiment with the correlation gradient applied along $z$, over an $x$–$y$–$z$ grid of $64 \times 64 \times 64$ points representing a box of $3 \times 3 \times 2.3$ mm$^3$ extent. A two-step phase cycle was applied to the first rf-pulse. $M^+$ is shown in au. (same scaling) after the $t_2$-interval summed over all $z$-slices. (a) Without additional dipole field, $t_1 = 2$ ms. (b) Additional dipole field at the centre of the box, $t_1 = 2$ ms. (c) As (b), $t_1 = 10$ ms. $M^+$ has grown significantly compared to (a and b), and the effect of the dipole is more pronounced than in (b).

CRAZED, or double-quantum-coherence-like, signal. As argued above, distant from the dipole near the edge of the cylinder, nearly the same signal intensity is observed with and without the dipole. Closer to the dipole, signal intensity is strongly reduced due to the local dipole field. Towards the edge of the cylinder, CRAZED signal decreases, reflecting the spatial distribution of $B_{DDF}$. The extent of the region of reduced signal close to the dipole is comparable to that observed for gradient echo images with comparable echo times (Figs. 2c and d). Signal intensity is far lower in the CRAZED experiment than in a gradient echo image. This can be seen when the CRAZED simulations of Fig. 3 are compared to the simulated CRAZED experiment without gradients (which basically yields the same signal as a gradient echo experiment) of Figs. 2c and d. During the very short $t_2$-interval, only small amounts of $M^+$ are refocused by the DDF. For longer $t_2$ more transverse magnetization is refocused and consequently a higher signal will be detected (Fig. 3c). On the other hand during the accordingly longer $t_1$-interval, dephasing of $M^+$ by $B_{dip}$ is more pronounced, dominating the effect of the applied gradient at distances further from the particle and the region of reduced signal consequently becomes larger. In the experimental implementation, maximum signal is obtained by allowing the signal to grow during the echo time, $TE$, of the spin-echo read out following the $t_2$-period (Fig. 1). Fig. 4 shows an experimentally acquired gradient echo image of a 0.5 mm-thick slice (a) and an experimental CRAZED image of a 1.0 mm slice (b) centred at the same position in the sample. Two prominent dark spots are observed in both images (arrows). In spin echo images, air bubbles of ca. 0.2 mm diameter at the centre of the slice and ca. 0.3 mm near the upper edge of the slice were identified as the sources of the upper-central, and central-right dark spots, respectively. In both images, further less pronounced dark spots were also observed. Most of these were also present in spin-echo images suggesting that only air bubbles and no single SPIOs used in the phantom were detected at the echo times employed here. However, the effects of the two large air bubbles were also detected with the CRAZED sequence. Taking into account the longer measurement time, direct application of CRAZED imaging did not yield advantages compared to gradient echo imaging in respect to detecting local dipolar fields.

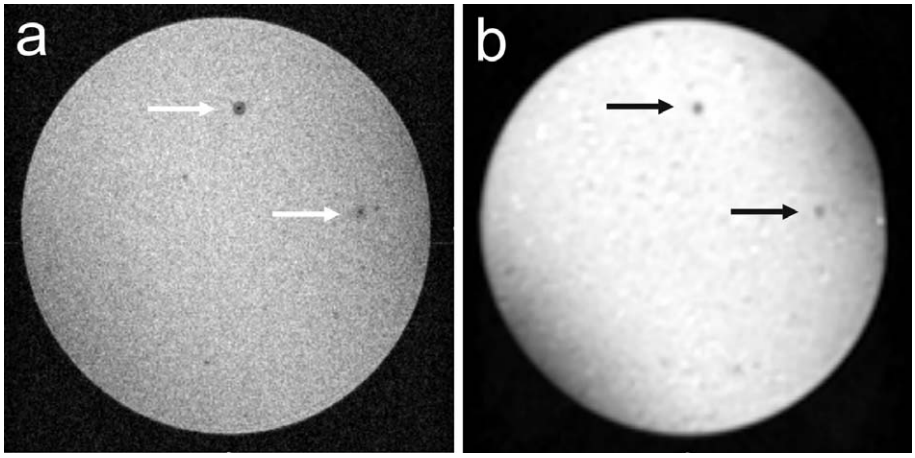


Fig. 4. (a) Gradient echo image of the gel phantom. Slice thickness: 0.5 mm, $TR/TE = 30/10$ ms, FOV $= (15\text{ mm})^2$, imaging matrix: $256^2$, 32 averages. (b) CRAZED image of a 1 mm slice centred at the same position of the phantom. $TR/TE = 10{,}000/40$ ms, FOV $= (15\text{ mm})^2$, imaging matrix: $128^2$, 4 averages. Arrows indicate regions of reduced signal from two air bubbles.

### 4.2. Positive contrast from local dipole fields

The CRAZED experiment, unlike conventional gradient echo imaging, offers the possibility of inverting the negative contrast. Positive contrast with more signal at the site of interest compared to surrounding areas can be achieved if the CRAZED experiment is performed with gradient modulation applied along the magic angle (we will keep the acronym CRAZED although no $z$-gradients are employed). In a homogeneous sample, application of magic angle gradients makes $B_{\mathrm{DDF}}$ vanish according to Eq. (4). In the presence of local dipole fields, $B_{\mathrm{dip}}$ interferes with $B_{\mathrm{DDF}}$ and can have two effects:

1. Locally the direction of the modulation is changed and may deviate from the magic angle. In this case signal from DQC will be detected.
2. $B_{\mathrm{dip}}$ may locally match the asymmetry of the correlation gradient pair and directly refocus SQC or SQC signal following other coherence pathways.

Fig. 5 shows the results of a simulation with gradient modulation applied along the magic angle. $M^+$ was summed over all $z$-slices, thus averaging out the modulation along the $z$-axis. The modulation of signal along the $x$-axis is still visible. In addition to this modulation, signal is also observed near the dipole, where evolution under the action of $B_{\mathrm{dip}}$ during the $t_1$-period interferes with the gradient modulation. The effect of the dipole is clearly visible in the simulation carried out without phase cycling (Figs. 5a and b): signal appears locally superimposed upon a lower background intensity. Figs. 5c and d show that use of a phase cycle suppresses the directly refocused signal. Signal does appear at the edge of the tube and near the dipole perturber, but the latter signal is reduced by more than a factor of ten after phase cycling. This suggests that the signal observed in Figs. 5a and b is mainly SQC-like since it does not follow the known behaviour of DQ-CRAZED signal [6,19,27]. For comparison with experimental data it is important to note that the image intensities shown in Figs. 5b and d would be averaged over several modulation lengths in each pixel of an experimentally acquired image. Fig. 6 shows corresponding experimental data. Several bright spots were observed, most of which could be matched with dark areas in high resolution spin echo images in corresponding or adjacent slices. The appearance and intensity of the bright spots was changed after phase cycling and overall lower signal intensities were observed (Fig. 6b).

The position of the dipole in the imaging slice has a significant influence on the signal that is generated. To demonstrate this effect, representative CRAZED images were calculated from the simulated data (shown in Fig. 5). Summation over 8 grid points was required to average out the

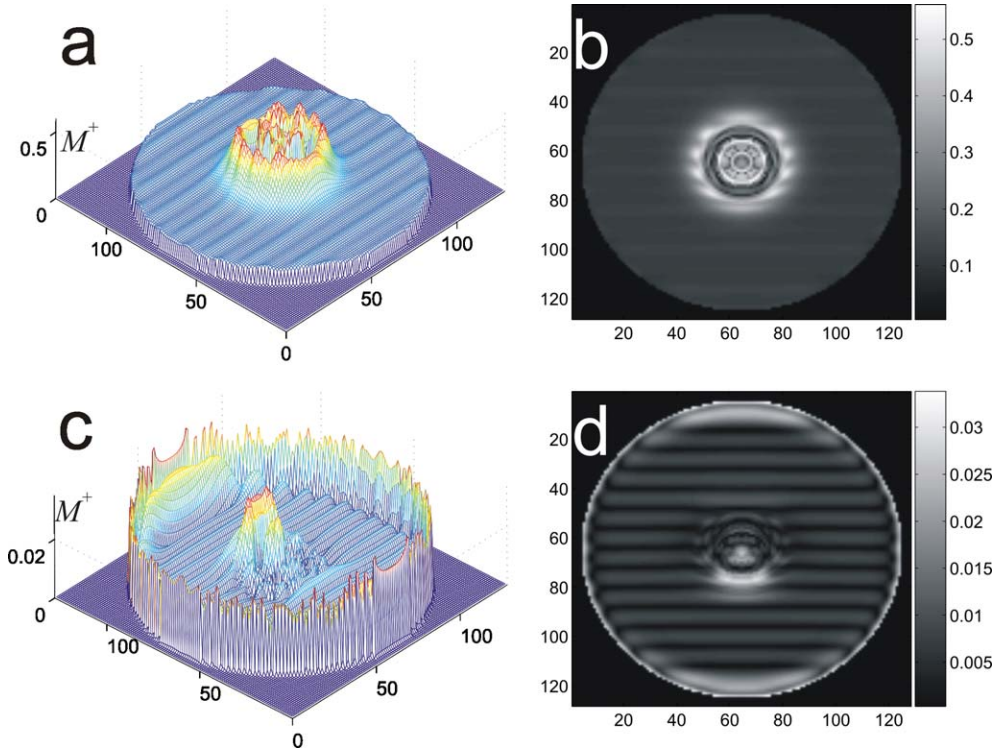


Fig. 5. Simulation of the CRAZED experiment with the correlation gradient applied along the magic angle, over an $x$–$y$–$z$ grid of $128 \times 128 \times 64$ points representing a box of size $(2.3\ \mathrm{mm})^3$, with $t_1 = 2$ ms. $M^+$ after the $t_2$-interval was summed over all $z$-slices, with no phase cycle (a and b), and after a two-step phase cycle $(x, -x)$ on the first rf-pulse (c and d). 3D plots of the absolute values of $M^+$ are shown in (a and c), the corresponding "images" in (b and d). The same scaling was used in all panels, $M^+$ shown in au. Note the reduced intensity after phase cycling.

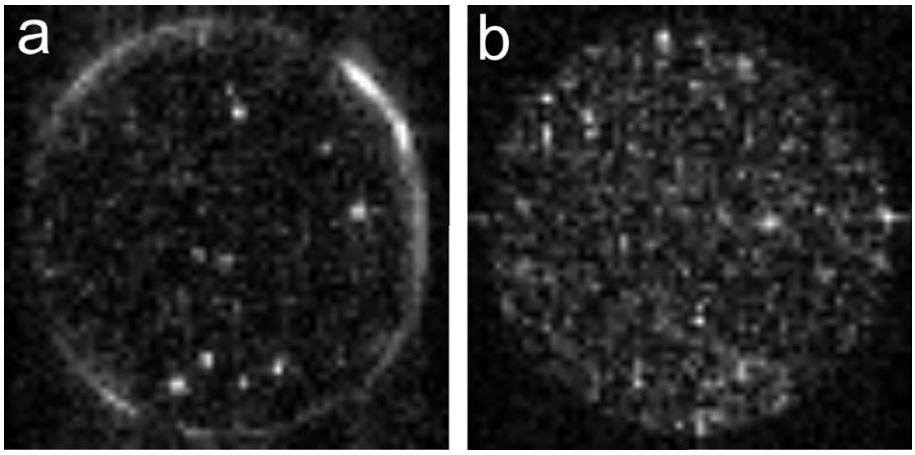


Fig. 6. (a) Magic angle CRAZED image of the same slice as shown in Fig. 4b. $t_1 = 4$ ms, $TR/TE = 3000/50$ ms, FOV $= (15\text{ mm})^2$, imaging matrix: $64^2$, 1 scan. (b) Magic angle CRAZED image as in (a), with two-step phase cycle $(x, -x)$ on the first rf-pulse. $t_1 = 3$ ms, 16 averages.

residual modulation of the magnetization imposed by the applied gradients. Thus $16 \times 16$ pixel images were obtained by summing over $8 \times 8$ grid points for each pixel. Images of 2.3 mm, or 1.15 mm thick slices were obtained by summing, respectively, over all 64 points in the slice direction, or over just the lower or upper 32 points. The resulting images are shown in Fig. 7, for the 2.3 mm slice (a and d), for the upper half of the simulated slice (b and e), and for the lower half (c and f). The effect of the interference of $B_{\text{dip}}$ with the CRAZED modulation depends on the position of the dipole with respect to the imaging slice. The appearance of the image close to the dipole is different in all calculated images and also changes with $t_1$ (data not shown). Figs. 7b and c illustrate that dipoles located in adjacent slices can also cause bright contrast in the image. The different appearance of the images obtained with and without phase cycling explains why varying changes in signal intensity are observed for different dipoles in Figs. 6a and b. Dipoles in the sample have different positions with respect to the imaging slice, thus leading to different changes in intensity occurring when phase cycling is employed.

A further CRAZED variant can also be used to produce positive contrast from local dipole fields. If the correlation gradient pulse pair does not have a ratio of areas of 1:2, no signal is detected in homogeneous parts of the sample. Dipole fields can locally refocus magnetization and

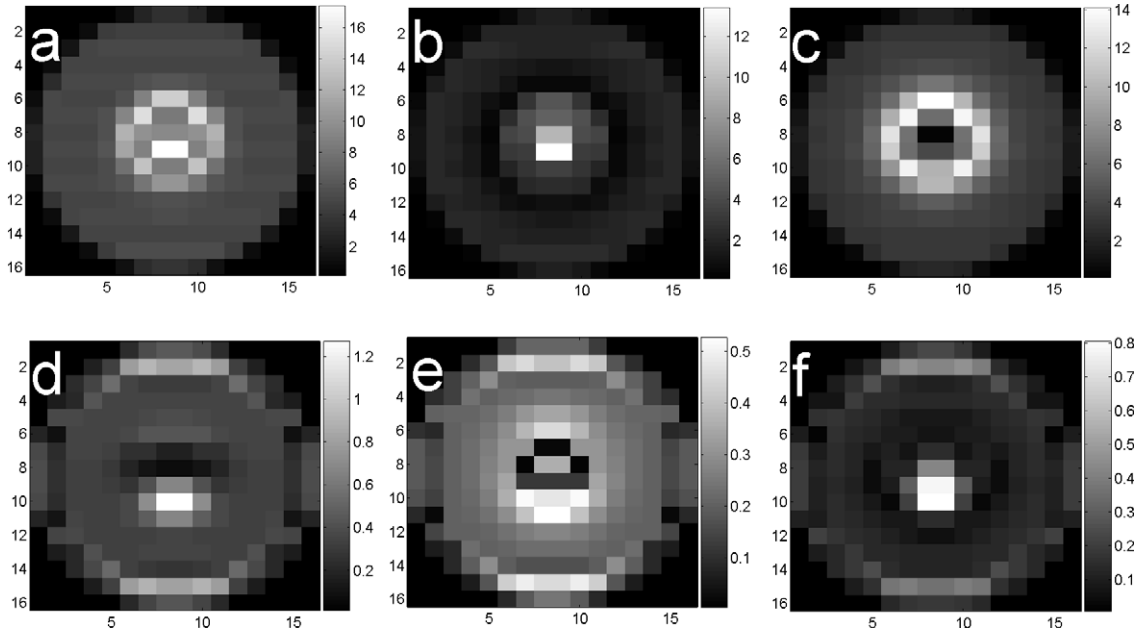


Fig. 7. Simulated magic angle CRAZED images calculated from the same data set as shown in Fig. 5, without phase cycling (a–c), and after a two-step phase cycle (d–f). Image intensity is shown in au. (same scaling in all panels). $M^+$ was summed over $8 \times 8$ pixels of the $128 \times 128$ matrix shown in Fig. 5 to generate each pixel of the $16 \times 16$ images shown here. $M^+$ was also summed over all $z$-slices to produce (a and d), over the upper 32 $z$-slices for (b and e), and over the lower 32 $z$-slices in for (c and f).

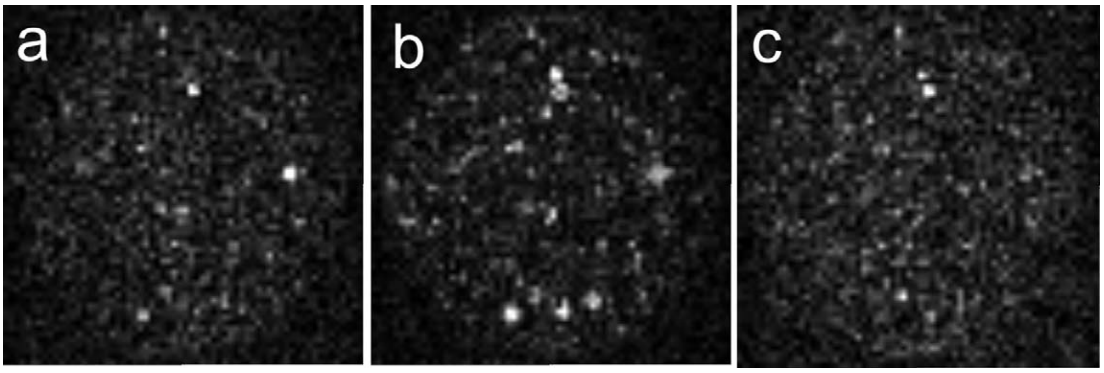


Fig. 8. Magic angle CRAZED images of the same slice as shown in Fig. 4b generated with mismatched correlation gradient pair. $TR/TE = 3000/40$ ms, FOV = $(15\text{ mm})^2$, imaging matrix: $64^2$, 1 scan. (a) $t_1 = 3$ ms, gradient area ratio 5:2. (b) $t_1 = 12$ ms, gradient area ratio 5:2. (c) $t_1 = 3$ ms, gradient area ratio 5:8.

produce signal over a dark background. Experimental images acquired from the same slice as in Fig. 6 are shown in Fig. 8 for different ratios of the two gradient pulse areas. Excellent suppression of the background signal is achieved and strong signals are observed without averaging. Varying the ratio of the areas of the two gradient pulses allows visualization of different dipoles (Figs. 8a and c). Increasing $t_1$ while the gradients are mismatched generates different patterns and changing intensities of signals from different dipoles (Figs 8a and b). Since $t_1$ can be varied and both the direction and ratio of the gradients can be adjusted, different dipoles could be selectively detected in this manner.

## 5. Discussion

CRAZED imaging can be used to visualize local dipole fields. In the normal CRAZED experiment, areas of reduced signal near the source of the dipole field are observed, similar to the effects manifested in gradient echo imaging experiments. While it was recently shown that CRAZED produces superior contrast in tissue with larger amounts of embedded nanoparticles [7], the effects of single sources of dipole fields are not more pronounced in the CRAZED experiment. Taking into account the fact that CRAZED usually yields lower SNR at lower resolution while requiring longer measurement times than gradient echo imaging, it becomes clear that imaging using the normal CRAZED sequence, is not the method of choice for visualizing local dipole fields in routine applications.

Small modifications to the CRAZED sequence allow for generation of strong positive contrast from local dipolar fields. Either the gradient modulation can be applied along the magic angle, or the two correlation gradient pulses can be mismatched. The results of our simulations for magic angle modulation suggest that most of the detected signal comes from directly refocused magnetization or intermolecular SQCs. Experimental data obtained with phase cycling corroborate this finding. The remaining signal observed after phase cycling shows that there is a small, but still significant contribution from DQC signal. Simulations were limited in maximum matrix size (resolution) and signal evolution time by the CPU-time required. Therefore, evolution during the spin echo read out was not included in the simulations and the gradient-imposed modulation lengths were larger than in the experiments. These two factors may explain why simulations do not fully match the experimental data. The observations that phase cycling dramatically changes the appearance of images and that the signal is dependent on the position of the dipole with respect to the imaging slice are reproduced by our simulations.

Compared to the previously presented method termed the ''white marker phenomenon'' [3] or ''bright iron effect'' [4], CRAZED requires longer measurement times, but offers excellent suppression of background signal that is extremely hard to achieve with the other methods. An alternative approach to visualizing local dipole fields with positive contrast used frequency selective refocusing of off-resonance magnetization, caused by the dipole [5]. This method also provides very good background suppression. Due to long $TR$ required by the use of spin echo imaging, measurement times were comparable to the CRAZED experiments used here. Beyond merely visualizing local dipole fields CRAZED imaging with deliberately mismatched gradient pairs may offer the unique possibility of producing detailed maps of local dipole fields, while providing efficient suppression of unwanted background signal. Similar to the proposed vector field imaging technique [30], these CRAZED variants might be used for dipole field mapping. A pre-requisite for this application will be a more detailed understanding of the dynamics of the signal in presence of significant dipole fields.

## 6. Conclusion

We have shown that CRAZED imaging can be used to visualize local dipole fields. With gradient modulation applied along the magic angle or mismatched coherence-selection gradients, positive contrast from local dipole fields can be created. Excellent suppression of the background

and sufficient signal from the dipoles can be achieved in short experimental times. Although no exact solution for signal evolution was found, the method may be a valuable tool for the investigation of experimentally created dipole fields, such as iron-labelled cells or targets in molecular imaging.

## Acknowledgments

This work was supported by Grants from the Deutsche Forschungsgemeinschaft (DFG, Fa474/1), DAAD (PPP/ARC program), and a Senior Mansfield Fellowship. The 750 MHz spectrometer was funded by the DFG (Ha1232/13).

## References

[1] P. Foster-Gareau, C. Heyn, A. Alejski, B.K. Rutt, Imaging single mammalian cells with a 1.5 T clinical MRI scanner, Magn. Reson. Med. 49 (2003) 968–971.
[2] K.A. Hinds, J.M. Hill, E.M. Shapiro, M.O. Laukkanen, A.C. Silva, C.A. Combs, T.R. Varney, R.S. Balaban, A.P. Koretsky, C.E. Dunbar, Highly efficient endosomal labeling of progenitor and stem cells with large magnetic particles allows magnetic resonance imaging of single cells, Blood 102 (2003) 867–872.
[3] J.H. Seppenwoolde, M.A. Viergever, C.J. Bakker, Passive tracking exploiting local signal conservation: the white marker phenomenon, Magn. Reson. Med. 50 (2003) 784–790.
[4] K.H. Hiller, C. Faber, T. Neuberger, S. Kohler, A. Stroh, C. Zimmer, P. Jakob, Magnet-Resonanz-Tomographie: Möglichkeiten der molekularen Bildgebung, Z. Med. Phys. 15 (2005) 155–162.
[5] C.H. Cunningham, T. Arai, P.C. Yang, M.V. McConnell, J.M. Pauly, S.M. Conolly, Positive contrast magnetic resonance imaging of cells labeled with magnetic nanoparticles, Magn. Reson. Med. 53 (2005) 999–1005.
[6] W.S. Warren, W. Richter, A.H. Andreotti, B.T. Farmer II, Generation of impossible cross-peaks between bulk water and biomolecules in solution NMR, Science 262 (1993) 2005–2009.
[7] K.L. Shannon, R.T. Branca, G. Galiana, S. Cenzano, W. Soboyevo, W.S. Warren, Simultaneous acquisition of multiple orders of intermolecular multiple-quantum coherence images in vivo, Magn. Reson. Imaging 22 (2004) 1407–1412.
[8] G. Deville, M. Bernier, J.M. Delrieux, NMR multiple echoes observed in solid 3He, Phys. Rev. B. 19 (1979) 5666–5688.
[9] J.P. Marques, R. Bowtell, Application of a Fourier-based method for rapid calculation of field inhomogeneity due to spatial variation of magnetic susceptibility, Conc. Magn. Reson. B. 25 (2005) 65–78.
[10] R. Bowtell, P. Robyr, Structural investigations with the dipolar demagnetizing field in solution NMR, Phys. Rev. Lett. 76 (1996) 4971–4974.
[11] P. Robyr, R. Bowtell, Nuclear magnetic resonance microscopy in liquids using the dipolar field, J. Chem. Phys. 106 (1997) 467–476.
[12] C. Ramanathan, R. Bowtell, NMR imaging and structure measurements using the long-range dipolar field in liquids, Phys. Rev. E 66 (2002) 041201,1-10.
[13] X.-P. Tang, C.-L. Chin, L.-S. Bouchard, F.W. Wehrli, W.S. Warren, Observing Bragg-like diffraction via multiple coupled nuclear spins, Phys. Lett. A 326 (2004) 114–125.
[14] R. Bowtell, R.M. Bowley, P. Glover, Multiple spin echoes in liquids in a high magnetic-field, J. Magn. Reson. 88 (1990) 643–651.
[15] Q. He, W. Richter, S. Vathyam, W.S. Warren, Intermolecular multiple-quantum coherences and cross correlations in solution nuclear magnetic resonance, J. Chem. Phys. 98 (1993) 6779–6800.
[16] W.S. Warren, S. Ahn, M. Mescher, M. Garwood, K. Ugurbil, W. Richter, R.R. Rizi, J. Hopkins, J.S. Leigh, MR imaging contrast enhancement based on intermolecular zero quantum coherences, Science 281 (1998) 247–251.
[17] Z. Chen, S.D. Kennedy, J. Zhong, Theoretical formalism and experimental confirmation of intermolecular dipolar effects under time-averaged magnetic field gradient, Chem. Phys. Lett. 313 (1999) 217–224.
[18] J. Zhong, Z. Chen, E. Kwok, New image contrast mechanisms in intermolecular double-quantum coherence human MR imaging, J. Magn. Reson. Imaging 12 (2000) 311–320.
[19] C. Ramanathan, R. Bowtell, Dynamics of the nuclear magnetic resonance COSY-revamped by asymmetric $z$-gradients (CRAZED) experiment, J. Chem. Phys. 114 (2001) 10854–10859.
[20] R. Bowtell, S. Gutteridge, C. Ramanathan, Imaging the long-range dipolar field in structured liquid state samples, J. Magn. Reson. 150 (2001) 147–155.
[21] S.S. Velan, P.T. Narasimhan, R.E. Jacobs, MR imaging with phase encoding of intermolecular multiple quantum coherences, J. Magn. Reson. 152 (2001) 189–194.
[22] L.S. Bouchard, R.R. Rizi, W.S. Warren, Magnetization structure contrast based on intermolecular multiple-quantum coherences, Magn. Reson. Med. 48 (2002) 973–979.
[23] S.M. Brown, P.N. Sen, D.G. Cory, Nuclear magnetic resonance scattering across interfaces via the dipolar demagnetizing field, J. Chem. Phys. 116 (2002) 295–301.
[24] S.M. Brown, P.N. Sen, D.G. Cory, Scaling laws in NMR scattering via dipolar fields, J. Magn. Reson. 154 (2002) 154–156.
[25] C.L. Chin, C. Tang, L.S. Bouchard, P.K. Saha, W.S. Warren, F.W. Wehrli, Isolating quantum coherences in structural imaging using intermolecular double-quantum coherence MRI, J. Magn. Reson. 165 (2003) 309–314.
[26] P.L. de Sousa, D. Gounot, D. Grucker, Flow effects in long-range dipolar field MRI, J. Magn. Reson. 162 (2003) 356–363.
[27] J.P. Marques, R. Bowtell, Optimizing the sequence parameters for double-quantum CRAZED imaging, Magn. Reson. Med. 51 (2004) 148–157.
[28] C.A. Corum, A.F. Gimtro, Spatially varying steady state longitudinal magnetization in distant dipolar field-based sequences, J. Magn. Reson. 171 (2004) 131–134.
[29] L.S. Bouchard, F.W. Wehrli, C.L. Chin, W.S. Warren, Structural anisotropy and internal magnetic fields in trabecular bone: coupling solution and solid dipolar interactions, J. Magn. Reson. 176 (2005) 27–36.
[30] L.S. Bouchard, W.S. Warren, Multiple-quantum vector field imaging by magnetic resonance, J. Magn. Reson. 177 (2005) 9–21.
[31] T. Enss, S. Ahn, W.S. Warren, Visualizing the dipolar field in solution NMR and MR imaging: three-dimensional structure simulation, Chem. Phys. Lett. 305 (1999) 101–108.
[32] S. Garett-Roe, W.S. Warren, Numerical studies of intermolecular multiple quantum coherences: high-resolution NMR in inhomogeneous fields and contrast enhancement in MRI, J. Magn. Reson. 146 (2000) 1–13.
[33] Y.Y. Lin, N. Lisitza, S. Ahn, W.S. Warren, Resurrection of crushed magnetization and chaotic dynamics in solution NMR, Science 290 (2000) 118–121.
[34] S.Y. Huang, Y.Y. Lin, N. Lisitza, W.S. Warren, Signal interferences from turbulent spin dynamics in solution nuclear magnetic resonance spectroscopy, J. Chem. Phys. 116 (2002) 10325–10337.
[35] C. Cai, Z. Chen, S. Cai, J. Zhong, A simulation algorithm based on Bloch equations and product operator matrix: application to dipolar and scalar couplings, J. Magn. Reson. 172 (2005) 242–253.
[36] C. Cai, Z. Chen, S. Cai, L.P. Hwang, J. Zhong, Finite difference simulation of diffusion behaviors under inter- and intra-molecular multiple-quantum coherences in liquid NMR, Chem. Phys. Lett. 407 (2005) 438–443.